CRYSTAL GROWTH & DESIGN

pubs.acs.org/crystal

Article

Thermodynamic and Kinetic Modulation of Methylammonium Lead Bromide Crystallization Revealed by In Situ Monitoring

Amnon G. Ortoll-Bloch, Ying Chen, Emily Hiralal, Nancy M. Washton, Karl T. Mueller, James De Yoreo, Jinhui Tao,* and Lara A. Estroff*

Cite This: *Cryst. Growth Des.* 2024, 24, 4955−4965

Read Online

ACCESS | Metrics & More | Article Recommendations | Supporting Information

ABSTRACT: Hybrid organic−inorganic perovskite (HOIP) crystals are promising optoelectronic materials, but little is known about either the thermodynamic and kinetic controls on crystal growth or the underlying growth mechanism(s). Herein, we use fluid-cell atomic force microscopy (AFM) and solution nuclear magnetic resonance (NMR) spectroscopy to investigate the growth of the model HOIP crystal $CH_3NH_3PbBr_3$ ($MAPbBr_3$) and to determine how formic acid (HCOOH) modulates the thermodynamics and kinetics of growth. The results show that growth of $MAPbBr_3$ in dimethylformamide (DMF) proceeds through the classical pathway by the spreading of molecular crystal steps generated at screw dislocations on the {100} surface. Temperature-dependent step velocity measurements demonstrate that with increasing concentration, HCOOH decreases the solubility of $MAPbBr_3$. From the AFM data, we also determine the apparent kinetic coefficient (β) of step movement as a function of HCOOH concentration. ^{1}H NMR measurements indicate that HCOOH increases the lifetime of the methylammonium (MA^+) ions and promotes the association of $MAPbBr_3$, thus tuning the solubility of the perovskite. We further propose that HCOOH alters the molecular tumbling motion and bulk diffusion of the MA^+ ions, possibly via H-bonding. Our findings establish a direct correlation between the mesoscale crystal growth kinetics and the molecular-scale interactions between organic additives and constituent ions, providing unprecedented insights for developing predictive syntheses of HOIP crystals with defined size, crystal habit and shape, and defect distribution.

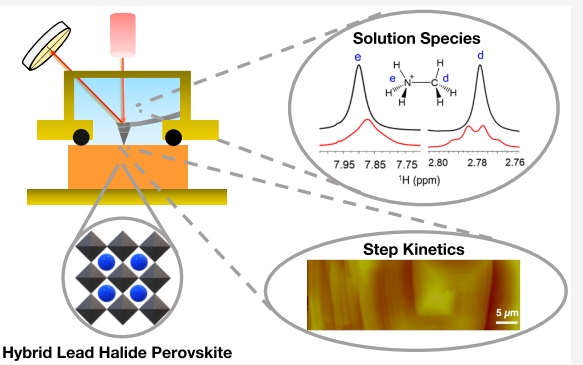

1. INTRODUCTION

Hybrid organic−inorganic perovskites (HOIPs), such as methylammonium lead bromide ($CH_3NH_3PbBr_3$; $MAPbBr_3$), are promising candidate materials for a variety of optoelectronic applications due to their desirable properties and solution processability. HOIPs are best known for their impressive breakthrough in photovoltaic technology: in less than ten years since their discovery, the power conversion efficiencies of perovskite solar cells have increased from 14% to over 25%, to rival efficiencies of silicon.[1] Although most research has centered around devices based on polycrystalline thin films of HOIPs, single crystals remain superior in terms of charge-carrier lifetimes, mobilities, and diffusion lengths.[2−5] Notably, single-crystal-based solar cells have shown promise in pushing perovskite photovoltaics toward the maximum theoretical efficiency defined by the Shockley−Queisser limit.[6,7] HOIP single crystals are also attractive as photosensors[8] and for γ- and X-ray detection due to their high detection efficiencies and wide bandgaps.[9,10] Optimizing the solution growth of HOIP crystals is crucial for further progress in both thin-film and single-crystal applications.[5] Such synthetic optimizations require a molecular-level understanding of the underlying mechanisms that govern HOIP crystal growth. This insight, however, is currently lacking. In this work, we investigate the thermodynamics and kinetics of $MAPbBr_3$ crystal growth with molecular-level resolution by in situ monitoring.

HOIP crystals are commonly grown by inverse-temperature crystallization (i.e., by heating a solution of the lead and organic salts to trigger nucleation) due to their apparent inverse solubility in certain organic solvents, such as dimethylformamide (DMF), due to temperature-triggered decomposition of the solvent to create acidic products.[11−16] Multiple solution species, including ion-complexes,[17−22] lead halide clusters and colloids,[23,24] and solid-state intermediates,[25−27] have been proposed as important components in the crystallization pathways for HOIPs. For example, researchers have proposed that heating is required to dissociate lead−solvent complexes and make the solution more supersaturated

Received: January 3, 2024
Revised: May 16, 2024
Accepted: May 17, 2024
Published: May 30, 2024

https://doi.org/10.1021/acs.cgd.4c00008
Cryst. Growth Des. 2024, 24, 4955−4965

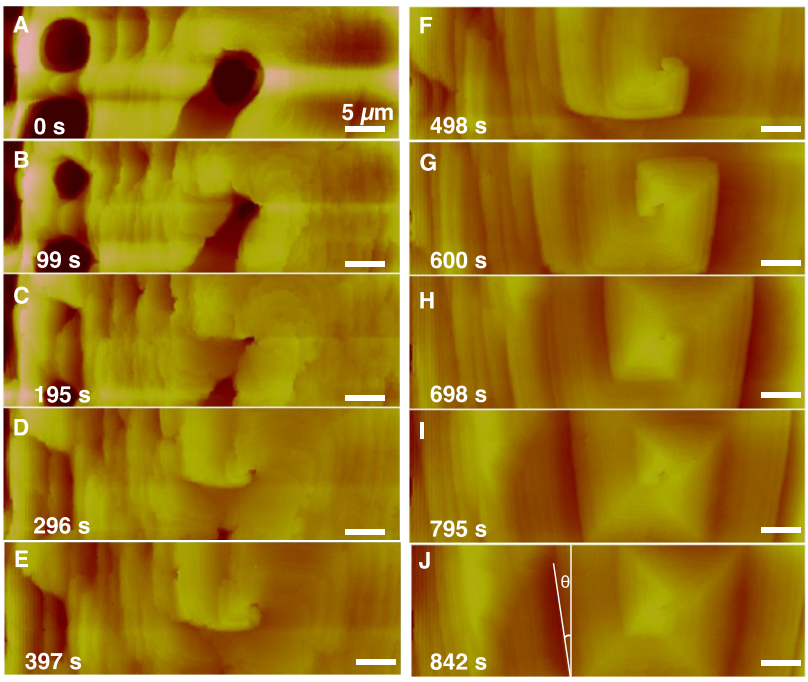

Figure 1. Series of time-resolved in situ AFM height images of a $MAPbBr_3$ surface exposed to a 0.94 M $PbBr_2$/MABr growth solution in DMF with 1.43 M HCOOH at 29 °C. All scale bars are 5 μm. The initial surface shows etch pits (A–D) that are subsequently filled. The growth of a specific hillock was monitored (E–J), with a measured step velocity of 27.6 ± 2.2 nm s^{-1}. The angle θ (J), measured between the step edges of the hillock and the vertical direction, was used to calculate the step velocity for the step trains on both sides of the hillock.

with respect to the perovskite.[11,12] Other work using light scattering techniques indicates that colloidal aggregates form in HOIP reagent solutions at room temperature.[13] As the temperature increases, these colloids dissolve, upon which the perovskite nucleates and grows. These findings suggest that these colloids have an "off-pathway" role in HOIP crystallization, meaning they are not the growth units of HOIP crystals. Instead, data suggest that colloids need to dissolve to provide solution species that do have "on-pathway" roles and directly act as growth units. Despite these insights, the pathways involved in the inverse-temperature crystallization of HOIPs remain elusive due to the lack of characterization techniques with high spatiotemporal resolution. Further investigating HOIP inverse-temperature crystallization pathways and kinetics will help gain precise control over final crystal size, crystal habit and shape, and even defect distribution, which are critical bottlenecks limiting the development of both thin-film and single-crystal-based devices.

Numerous additives have been reported to affect HOIP crystal growth. Both organic and inorganic acids have been utilized as additives for HOIP crystallization.[28−30] For example, amino acids have been reported to incorporate into the HOIP crystal lattice, causing lattice distortions and changes to the optical bandgap.[30] Most of the inorganic acids introduce undesired impurities into the final perovskite product. For example, halide and hypophosphoric acids can lead to the incorporation of excess halide and phosphorus, respectively, into the final HOIP films.[31] In contrast, an organic acid, formic acid (HCOOH), does not become incorporated and aids in the formation of pinhole-free films with larger, highly oriented crystalline domains, which lead to high-performance devices.[31] As an additive for inverse-temperature crystallization, it is proposed that HCOOH lowers the onset temperature for crystallization by promoting the dissociation of intermediate colloidal particles and the concomitant formation of solution species necessary for crystallization.[13,31] Reducing the temperatures required for crystal growth could help prevent surface degradation, which has been observed for $MAPbI_3$.[32] Additionally, lower growth temperatures and slower crystal growth rates decrease defect densities in $MAPbBr_3$ single crystals, leading to superior optoelectronic properties as compared to single crystals grown at higher temperatures.[33]

Additives can change the kinetic coefficient of step movement (β) in multiple ways, including altering the kink number density and interfering with the solvation shell of the growth unit and the growth sites.[34−40] Multiple parameters, including the additive's molecular size, charge, and hydrophilicity, have proven to be critical in tuning the kinetic coefficient.[41,42] Kinetic coefficients can be determined from in situ atomic force microscopy (AFM) measurements of step velocity collected at different supersaturations under constant temperature. In situ AFM has been extensively used to directly observe crystal growth and dissolution dynamics for a variety of materials, ranging from inorganic geologic minerals and biominerals to proteins and functional crystals.[35,36,43−52] By measuring step kinetics and step morphologies in various solution conditions, this approach can help elucidate the mechanisms that govern additive−crystal interactions. Herein, in situ AFM is employed to quantify the effects of HCOOH concentration on the solubility and the kinetic coefficient of $MAPbBr_3$ during mesoscale crystal growth. These crystal growth kinetics measurements are complemented by solution ^{1}H NMR measurements to gain insight into molecular-level changes in solution speciation caused by HCOOH and the relationship of those changes to the growth kinetics.

https://doi.org/10.1021/acs.cgd.4c00008
Cryst. Growth Des. 2024, 24, 4955−4965

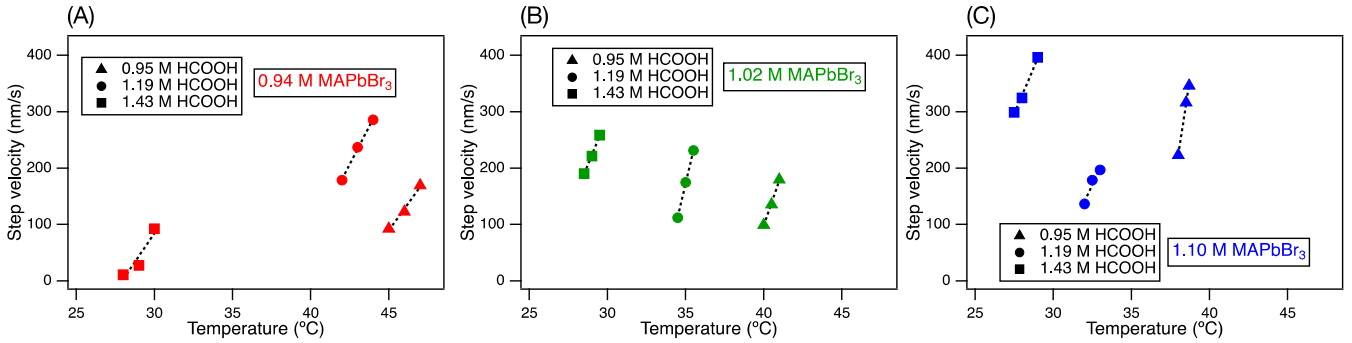

Figure 2. (A) Step velocity data as a function of temperature for solution compositions with 0.94 M $MAPbBr_3$. (B) Step velocity data as a function of temperature for solution compositions with 1.02 M $MAPbBr_3$. (C) Step velocity data as a function of temperature for solution compositions with 1.10 M $MAPbBr_3$. Marker shape corresponds to HCOOH concentration: triangles are for 0.95 M HCOOH, circles are for 1.19 M HCOOH, and squares are for 1.43 M HCOOH. Marker color corresponds to $MAPbBr_3$ concentration: red is for 0.94 M $MAPbBr_3$, green is for 1.02 M $MAPbBr_3$, and blue is for 1.10 M $MAPbBr_3$. Error bars are smaller than the size of data points. Black dashed lines correspond to the best line fit for each composition's data set. See Table S1 for line fit results.

2. RESULTS AND DISCUSSION

HOIPs, including $MAPbBr_3$, are highly soluble materials, especially at room temperature,[12,53] and their crystallization requires the use of organic solvents at elevated temperatures,[54,55] antisolvents,[56] or concentrated HBr[57] to achieve high-quality single crystals or thin films. These experimental factors present a substantial challenge when performing in situ AFM measurements for two reasons. First, crystal growth rates roughly scale with solubility under conventional synthesis conditions.[35] HOIP crystals grow rapidly, exhibiting step rates that quickly become too fast to measure by conventional fluid-cell AFM as the supersaturation is increased from zero. By carefully tuning the temperature to achieve near-equilibrium solution conditions, however, we were able to use AFM to observe growth hillocks on the {100} facet of an $MAPbBr_3$ single crystal and track the growth and dissolution dynamics in the spiral growth regime. Second, these hot organic solutions must be maintained at constant conditions during AFM measurements. To keep the conditions manageable, given the high equilibrium temperature (T_e) for $MAPbBr_3$ growth in DMF in the absence of additives, adding HCOOH to the growth solutions was also necessary to successfully track the growth process. For this study, we maintained a 1-to-1 $PbBr_2$/MABr molar ratio and selected three $PbBr_2$ concentrations (0.94, 1.02, and 1.10 M) and three HCOOH concentrations (4, 5, and 6% by volume ratio to DMF, or 0.95, 1.19, and 1.43 M HCOOH, respectively) for each $PbBr_2$ concentration.

Millimeter-sized $MAPbBr_3$ seed crystals were grown in a 1 M $PbBr_2$/MABr solution that was heated to 80 °C according to previously published methods.[11,14] $MAPbBr_3$ has a cubic crystal structure, and cuboid crystals with six equivalent {100} facets were obtained (Figure S1).[58] For our AFM experiments, we imaged one of the two largest exposed {100} facets. To observe the propagation of crystal steps on these hillocks, we first estimated the approximate T_e for each overgrowth solution composition by tuning the temperature and using optical microscopy to search the surface for dissolution pits or growth hillocks (Figure S2). At temperatures below T_e, we observed dissolution pits on the crystal surface (Figure 1A). These pits allowed for posterior monitoring of crystal growth because some dissolution pits will evolve into spiral growth hillocks at supersaturated conditions. When the temperature was raised above T_e, the etch pits were filled and numerous growth hillocks emerged (Figure 1B–D). Once a stable growth hillock was identified, we monitored the growth of that hillock at a constant temperature (Figure 1E–J).

For each solution composition, we determined the step velocities at three different temperatures (Figure 2). Step speeds were determined using standard methods (see Section 4). Our step velocity measurements show that increasing the HCOOH concentration leads to lower temperatures being required for crystal growth, in accordance with the literature.[13] Moreover, we found that, at a constant HCOOH concentration and within the same temperature range, as expected, the step velocity increases with increasing supersaturation, which is also consistent with the literature.[34,35,52] Fitting a line to the data set for each solution composition yielded good fits for all cases (all $R^2 > 0.894$, with an average R^2 from all fits equal to 0.979; Table S1). The quality of the line fits indicates that, over the narrow temperature range at which these measurements were carried out, the dependence of step velocity on temperature can be approximated by a linear dependence, even though we expect both β and the crystal solubility (C_e) to exhibit nonlinear dependencies over a sufficiently large range of temperature.[41,59]

Using the line fits from Figure 2 (Table S1), we obtained the equilibrium temperature, T_e, for each solution composition by extrapolating to the temperature at which the step velocity goes to zero ($v_s = 0$). We note that such extrapolation assumes a linear relationship between step velocity and growth temperature. Step velocities, however, might not follow this linear relationship under near-equilibrium conditions due to either impurity effects or changes in the internal step structure.[60] Using this assumption, at T_e, the $MAPbBr_3$ concentration used for the measurements corresponds to the equilibrium concentration (i.e., C_e) for that specific solution composition. With the T_e and C_e values for each composition, we generated a solubility curve for each HCOOH concentration (Figure 3) by fitting our data to the following eq (eq 1) derived from the van't Hoff equation:[16]

$$C_e = A \exp\left(\frac{B}{T_e}\right) \quad (1)$$

where C_e corresponds to the $MAPbBr_3$ solubility in mol/L (M), A is a parameter associated with the entropy of dissolution, B is a parameter associated with the enthalpy of dissolution, and T_e is the equilibrium temperature in Kelvin.

https://doi.org/10.1021/acs.cgd.4c00008
Cryst. Growth Des. 2024, 24, 4955−4965

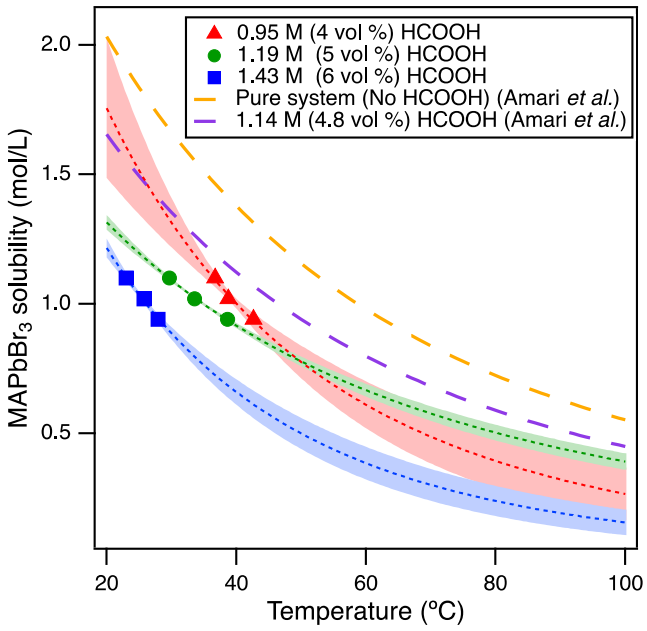

Figure 3. Solubility curves for $MAPbBr_3$ in DMF in the presence of varying concentrations of HCOOH. Experimentally determined data points from in situ AFM step velocity measurements are shown as solid data points. Error bars are smaller than the size of data points. Data were fit to eq 1 (dashed lines). One-standard-deviation confidence bands are shown for each fit. Two solubility curves from other work using bulk solubility measurements are included for comparison.[16]

Both *A* and *B* parameters were determined independently for each HCOOH concentration (Table S2). For reference, two solubility curves from other work,[16] one for the pure $MAPbBr_3$/DMF system and another for the 4.8 vol % (1.14 M) HCOOH system, are plotted along with our curves.

The values of C_e for $MAPbBr_3$ determined in this study as a function of HCOOH concentration originate from molecular-scale measurements of step dynamics on the {100} facet and are lower than those measured macroscopically. These discrepancies are expected due to the large experimental differences between the two approaches. While solubility is an equilibrium property of crystals in solution, the crystals need to evolve to express the equilibrium distribution of facet types and sizes for an accurate solubility to be measured. Macroscopic measurements entail the grinding of single crystals into powders.[16] Consequently, it is not surprising to observe differences between the two types of measurements. In order to extract the kinetic coefficients for the steps, however, we require the value of the concentration at which the step speed goes to zero, i.e., the ion attachment rate equals the detachment rate. Hence, the values determined here are the appropriate ones for our study, and the similar magnitude and temperature dependence to the macroscopic values lends confidence to those values.

These results, and those of others,[16] show that the solubility of $MAPbBr_3$ in DMF decreases with increasing HCOOH concentration (i.e., HCOOH shifts the thermodynamic equilibrium toward crystallization instead of dissolution). Other work has proposed that HCOOH helps dissolve colloids by catalyzing the hydrolysis of DMF, forming dimethylamine and increasing the solvating power of the DMF solvent.[13,31] Additionally, species (e.g., bromoplumbate complexes or single ions) produced by the dissolution of colloids could have "on-pathway" roles. For example, for crystallization to proceed, "off-pathway" colloidal particles might need to dissolve to provide solution species that act as the growth units and attach to the growing $MAPbBr_3$ crystal. Our AFM experiments, however, have limitations to visualize individual growth units directly, nor are they able to reveal dynamic processes of

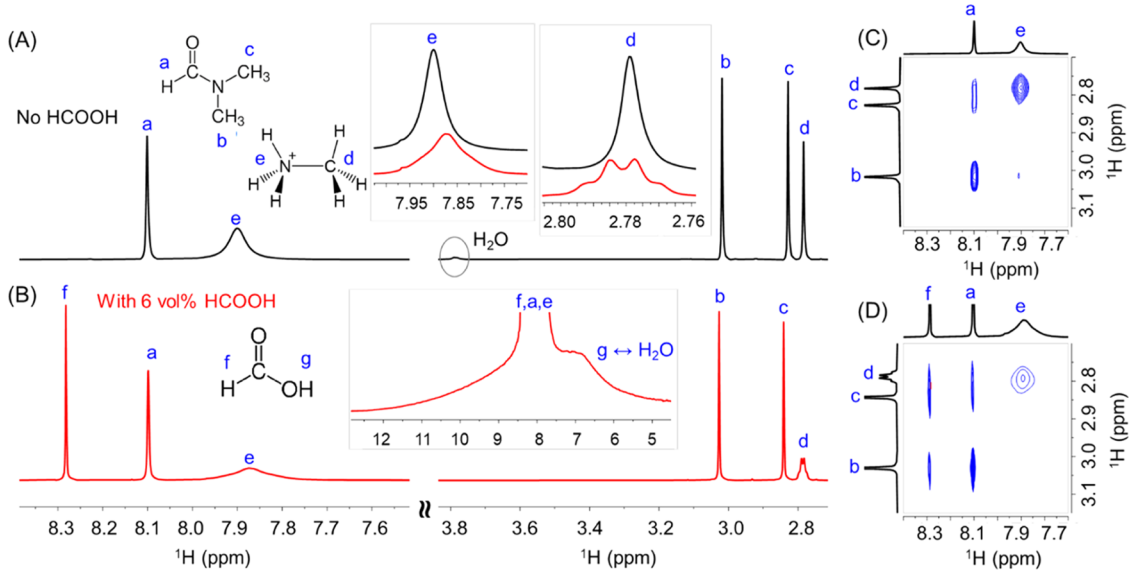

Figure 4. ^1H NMR spectra of (A) 1 M $PbBr_2$/MABr in DMF (black, top) and (B) with the addition of 1.43 M (6 vol %) HCOOH (red, bottom) at 25 °C. Insets in panel (A) are comparisons of the MA^+ NH_3^+ and MA^+ CH_3 resonances (top black curves without HCOOH; bottom red curves with HCOOH). The inset in panel (B) shows the broad peak between 5 and 12 ppm is a result of the fast exchange between HCOOH and water (see Figure S4 for full spectrum). 2D ^1H–^1H NOESY spectra of (C) 1 M $PbBr_2$/MABr in DMF and (D) with the addition of 1.43 M (6 vol %) HCOOH at 25 °C (see Figure S3 for full spectra). All protons are identified with lower-case letters (a–g), as shown on the chemical structures in panels (A) and (B). The proton lettering is used to assign peaks in (A)–(D).

https://doi.org/10.1021/acs.cgd.4c00008
Cryst. Growth Des. 2024, 24, 4955–4965

solution species occurring concomitantly with the attachment of growth units to the crystal surface.

Solution ^{1}H NMR is performed to further understand the effects of HCOOH on the behavior of species down to the molecular level. The results, described below, show that HCOOH increases the lifetime and the concentration of MA^+ ions and forms a strong H-bond network with both DMF molecules and MA^+ ions. Addition of 1.43 M HCOOH (6 vol %) at 25 °C to 1 M $PbBr_2$/MABr solutions in DMF leads to changes in the ^{1}H NMR spectra of the residual H_2O peak (water content varied from 0.1 to 0.7 M), as well as the NH_3^+ and CH_3 peaks from the MA^+ ions (Figure 4A,B). The observed changes are due to the differences in the lifetime of the $CH_3NH_3^+$ ions in the presence or absence of HCOOH. In the solutions without HCOOH, the $CH_3NH_3^+ + H_2O \rightleftharpoons CH_3NH_2 + H_3O^+$ equilibrium has an exchange rate of 1−100 s^{-1}, as estimated from the well-defined H_2O resonance at 3.8 ppm and the NH_3^+ signal at 7.9 ppm (Figure 4A) as well as the peak volumes of 2D ^{1}H−^{1}H NOESY spectrum (Figure S3 and see Section 4 for details).[61,62] Adding HCOOH causes the peak between 5 and 12 ppm to broaden (Figures 4B inset and S4) as a result of the much faster exchange associated with the deprotonation of HCOOH ($HCOOH + H_2O \rightleftharpoons HCOO^- + H_3O^+$). The poorly resolved triplet at 7.9 ppm of the NH_3^+ protons is caused by the residual J-coupling between ^{1}H and ^{14}N with $^1J_{N-H}$ of 27 Hz (Figure S5C). The lifetime of $CH_3NH_3^+$ is much longer in the presence of HCOOH than it is without, yielding a well-resolved quartet at 2.8 ppm due to the J-coupling between NH_3^+ and CH_3 with $^3J_{HNCH}$ = 5.7 Hz (Figure S5D). This analysis shows that, in room-temperature, HCOOH-containing solutions, the longer lifetime, and the associated higher concentration of $CH_3NH_3^+$ push the $MAPbBr_3$ solubility equilibrium toward the association of $CH_3NH_3^+$ and $[PbBr_n]^{2-n}$ required for $MAPbBr_3$ formation, as per Le Chatelier's principle. These observations are consistent with the solubility values from our AFM results, where increasing the HCOOH concentration decreases $MAPbBr_3$ solubility (Figure 3) and provide a molecular picture of why these solubility changes occur. Furthermore, 2D NOESY spectra exhibit the NOE cross-peaks between DMF-H_a and MA^+-H_d (Figures 4C and S3) and between HCOOH-H_f, MA^+-H_d, DMF-H_b, and DMF-H_c with the addition of HCOOH (Figure 4D), suggesting a close proximity (≲5 Å) between DMF, MA^+, and HCOOH in solution, which may be a direct result of the H-bond network among these species. In addition, 2D NOESY spectra also clearly show the chemical exchange between the b and c protons of DMF at 50 °C without HCOOH (Figure S7A), but this exchange is not detectable with 1.43 M (6 vol %) HCOOH (Figure S7B), indicating that the rotation of DMF is more restrained with HCOOH. This additional H-bond network with HCOOH may affect the kinetics of crystal growth.

Knowing that HCOOH affects the solubility of $MAPbBr_3$ from a thermodynamic viewpoint, we sought to elucidate the kinetic contributions of this additive to crystal growth. We use the relationship that correlates the step velocity with the supersaturation via the kinetic coefficient, β.[35] For a crystal growing by step flow, the step speed obeys the following eq (eq 2):[51]

$$v_s = \omega\beta(C - C_e) \quad (2)$$

where ω is the molecular volume of a growth unit (4.162×10^{-23} cm^3 for $MAPbBr_3$) and C is the actual $MAPbBr_3$ concentration at the crystal/solution interface. This expression separates out the impact of thermodynamic effects captured through the excess concentration ($C - C_e$) and the influence of kinetic processes contained in β. We note that if we use the bulk concentration and assume that the crystal growth is fully interface-controlled, eq 2 will yield an apparent kinetic coefficient. To obtain the "true" kinetic coefficient, we would need to have an accurate measurement of the surface concentration, which is experimentally challenging to determine.[60,63,64] Additionally, understanding the role of additives such as HCOOH in modulating local surface concentrations is nontrivial and will require future experiments. With these caveats in mind, we proceeded to evaluate the growth kinetics of $MAPbBr_3$ as a function of HCOOH concentration.

We determined the relationship between HCOOH concentration and the apparent kinetic coefficient, which we extracted from the step velocity data for the different HCOOH concentrations using eq 2. Given that β depends exponentially on temperature,[51] to make this comparison, we must represent the values of all of the step velocities and equilibrium concentrations at the same temperature. First, we extrapolated the step velocities and solubilities to 45 °C using the fits from Figures 2 and 3, respectively (Table S3). The higher temperature of 45 °C was selected to ensure that all of the step velocities are positive for all supersaturations and additive concentrations (Figure 2). The resulting step velocities as a function of $C - C_e$ are shown in Figure S6. Based upon the calculated apparent kinetic coefficients for each HCOOH concentration from the slopes in Figure S6 (Table S3), we report a range of values from 0.012−0.042 cm/s.

This range of values for the apparent kinetic coefficient are consistent with that of other crystals—smaller than the values for simple ionic crystals with high solubilities but larger than macromolecular crystals—and exhibit the general trend among crystals of increasing kinetic coefficient with increasing solubility.[36] Although the interplay between organic additive concentration, temperature, and crystallization pathways of HOIP single crystals has not been systematically probed,[30,65] the role of crystal growth additives, including ions, small organic molecules, proteins, and polymers, has been studied for numerous other systems.[42,52] Such studies have shown that additives can modify crystal growth via several mechanisms:[35,36,66] inhibition of step movement by adsorbing at step edges or kink sites and generating step-pinning or kink-blocking sites,[44,67,68] action as surfactants that change step and/or interfacial energies,[69] incorporation into the lattice and thus changing the solubility of the crystal,[70] and even introduction of stress into the crystal lattice or step edges.[44,71] Each of these mechanisms impacts the net rate at which growth units are added to the advancing steps as compared to that of additive-free growth.[72] This rate is given by the kinetic coefficient, β, which in turn is related to several processes, including the kink number density, the local diffusivity, and the activation barrier to growth, which stems from solute desolvation, adsorption, diffusion, and incorporation into the growing crystal.[35,45,60,67] β has been proposed to be dominated by the restructuring of the solvation shell as the growth unit approaches the growth front.[34,49] As such, measured kinetic coefficients vary as a function of crystal type (ionic vs small molecule vs protein) as well as solvent (aqueous vs organic) and growth mechanism (ion-by-ion vs larger growth units).[36]

https://doi.org/10.1021/acs.cgd.4c00008
Cryst. Growth Des. 2024, 24, 4955−4965

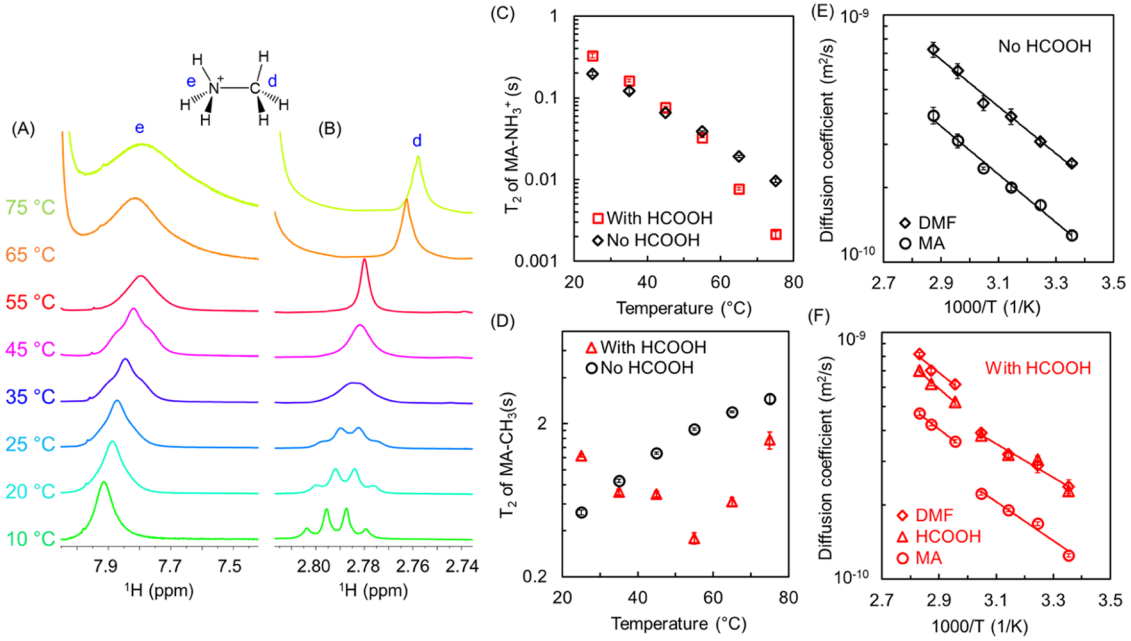

Figure 5. ^{1}H NMR spectra of MA$^+$ NH_3^+ (A) and MA$^+$ CH_3 (B), and ^{1}H spin−spin relaxation time constant T_2 of MA$^+$ NH_3^+ (C) and MA$^+$ CH_3 (D) in 1 M $PbBr_2$/MABr in DMF with the addition of 1.43 M (6 vol %) HCOOH as the temperature was increased from 10 to 75 °C (See Figure S8 for full spectra). Arrhenius plots of diffusion coefficients estimated from ^{1}H pulsed-field gradient (PFG) NMR in (E) 1 M $PbBr_2$/MABr in DMF and (F) 1 M $PbBr_2$/MABr in DMF with 1.43 M (6 vol %) HCOOH. Error bars were obtained by fitting the experimental data to the single-component exponential decay equation for T_2 ($I = I_0 \exp(-\tau/T_2)$) and to the Stejaska−Tanner eq (eq 4 in Materials and Methods) for diffusion coefficients. Activation energy of diffusion, E_a, values are extracted from the Arrhenius equation, $D = D_0 e^{-E_a/RT}$, where D_0 is the pre-exponential factor, R is the gas constant, and T is the absolute temperature.

In the current study, both the magnitude of the calculated kinetic coefficients (~10^{-2} cm/s) and the trend in decreasing kinetic coefficient value with increasing [HCOOH]—and decreasing solubility—can provide insight into the growth of $MAPbBr_3$. Importantly, we are evaluating the growth of an ionic crystal from an organic solvent, DMF. Solvation energies of organic and inorganic ions in different solvents vary as a function of ionic size, ionic charge, and solvent, with larger solvation energies for smaller inorganic ions in water as compared to larger organic ions in organic solvents.[73−75] The decreasing trend in β at higher HCOOH concentrations suggests that the HCOOH inhibits the step growth of $MAPbBr_3$. We were not able to collect data for the pure system (without HCOOH) because the temperature range in which the pure system will grow is higher than the temperature control available with our existing heating stage. Based upon the observed trend, however, we can predict that in the absence of HCOOH, β would be even larger, indicating a faster attachment of growth units in the pure system. We emphasize that these observations are counterintuitive: a lower solubility due to HCOOH addition indicates an increased relative stability of the perovskite crystals, which we would expect to lead to faster (not slower) growth kinetics, as formalized by the Berthollet rule.[50,76] This apparent violation to the Berthollet rule might indicate unusual additive incorporation kinetics due to the thermodynamic factor counteracting the kinetic factor during this crystal growth.

Given the importance of solvation/desolvation kinetics in determining both the solubility and the kinetic coefficient, we again turn to NMR for molecular insights into these trends. Variable temperature solution NMR relaxation measurements were used to probe the solution dynamics that underlie the decreasing trend in the kinetic coefficient with increasing HCOOH concentration. In HCOOH-containing solutions, increasing the temperature from 10 to 45 °C leads to changes in the resolution of the NH_3^+ triplet (~7.9 ppm, Figure 5A) and the CH_3 quartet (~2.8 ppm, Figure 5B), i.e., the NH_3^+ triplet becomes better resolved with increasing temperature, while the CH_3 quartet becomes less resolved with increasing temperature (Figure S5). These changes suggest that, from 10 to 45 °C, HCOOH slows down the reorientation motion of MA$^+$ ions with increasing temperature. Additionally, the major ^{1}H spin−spin relaxation (T_2) mechanisms for the NH_3^+ moiety of MA$^+$ include the exchange between NH_3^+ and H_2O, the quadrupolar relaxation by ^{14}N, and the tumbling motion of the MA$^+$ ions. In contrast, ^{1}H T_2 of the CH_3 group of MA$^+$ is primarily determined by the tumbling reorientation of MA$^+$ ions.[77] As shown in Figure 5C, ^{1}H T_2 of the NH_3^+ group experiences a drop with increasing temperature, both in the presence and absence of HCOOH. This drop is mainly caused by the exchange with water, while the effect from the larger ^{14}N quadrupolar coupling and slower tumbling motion may add to the more rapid drop in the solution with HCOOH. In the absence of HCOOH, the ^{1}H T_2 of the CH_3 group monotonically increased with increasing temperature (Figure 5D). When HCOOH was added, however, the T_2 of the CH_3 group decreased with temperature, reaching a minimum at 55 °C (Figure 5D). One explanation for the hindered tumbling motion of the MA$^+$ ions in the presence of HCOOH is that the interactions between MA$^+$ ions and bromoplumbate complexes become stronger with increasing temperature. The smallest T_2 value of MA$^+$, observed at 55 °C, may be explained by the preorganization of ion associations of MA$^+$ and bromoplumbates in solution prior to nucleation.

We can also determine the translational motion (i.e., the diffusion coefficient D) in bulk solution from ^{1}H diffusion-

https://doi.org/10.1021/acs.cgd.4c00008
Cryst. Growth Des. 2024, 24, 4955−4965

ordered NMR spectroscopy (DOSY). In the absence of HCOOH, from 25 to 80 °C, the Arrhenius plot of $D(MA^+)$ and D(DMF) as a function of $1000/T$ results in a diffusion activation energy of 19 ± 1 and 18 ± 1 kJ/mol for MA^+ and DMF, respectively (Figure 5E). The sudden increase in the diffusion coefficients of DMF, MA^+, and HCOOH at temperatures above 55 °C indicates the onset of homogeneous $MAPbBr_3$ nucleation above 55 °C because the viscosity of the remaining solution drops dramatically as a result of reduced ion concentrations in the solution after nucleation. D(DMF) and D(HCOOH) are close in value from 25 to 55 °C (Figure 5F), likely due to the H-bond network formed from the association between HCOOH and DMF molecules. The addition of HCOOH reduces the activation energy of diffusion for DMF to 13 ± 2 kJ/mol and, to a lesser extent, for MA^+ to 15 ± 2 kJ/mol. More detailed experimental and simulation work is needed to unravel how HCOOH changes the growth kinetics by influencing the conformational freedom of solution species, solute desolvation, growth unit incorporation, and possible kink-blocking processes.

3. CONCLUSIONS

In conclusion, we established a quantitative understanding of the role of HCOOH in the crystallization of $MAPbBr_3$ single crystals in DMF by combining in situ AFM and variable temperature solution NMR. Our results demonstrate that HCOOH has at least a dual effect on $MAPbBr_3$ crystal growth. HCOOH decreases $MAPbBr_3$ solubility by enhancing the lifetime of MA^+ ions and shifting the chemical equilibrium toward the association of $MAPbBr_3$. Moreover, HCOOH appears to inhibit the molecular tumbling of MA^+ ions, which may in turn result in changes in the kinetic coefficient. Therefore, HCOOH alters both the thermodynamics and kinetics of $MAPbBr_3$ growth. While our experiments have focused on understanding solution speciation and crystallization of $MAPbBr_3$ using the inverse-temperature single-crystal growth method, our approaches and findings are also relevant for understanding crystallization of thin films using methods such as antisolvent quenching.[57] We note, however, that as compared to the near-equilibrium conditions used to achieve large single crystals, perovskite thin-film growth is often occurring far-from-equilibrium at high supersaturations. Additional studies are required to understand what other processes may be occurring in these cases. Unraveling the molecular role of additives in HOIP growth will help move forward the predictive design of additives to tailor the thermodynamics and kinetics of the synthesis of HOIP single crystals and thin films with improved crystal composition, size, habit, and defect distribution, all of which dictate the optoelectronic and energy conversion performances of HOIP-based devices.

4. METHODS

4.1. Materials. All materials were used as received. *N*,*N*′-dimethylformamide (DMF, anhydrous, 99.8%), lead(II) bromide ($PbBr_2$, 99.999%, trace metal basis), and HCOOH (HCOOH, 90%) were obtained from Sigma-Aldrich. Methylammonium bromide (MABr) was obtained from GreatCell Solar (formerly Dyesol; Australia).

4.2. Solution Preparation for AFM Measurements. Solutions (1 mL) of varying concentrations (0.94, 1, 1.02, and 1.1 M) of $PbBr_2$ and MABr in a 1-to-1 molar ratio were prepared by weighing the salts in air and adding the appropriate volumes of solvent and HCOOH. The salts were dissolved by stirring at room temperature until the solution was completely clear. The HCOOH concentrations used were 4, 5, and 6 vol % (i.e., 0.95, 1.19, and 1.43 M HCOOH).

4.3. Synthesis of $MAPbBr_3$ Single Crystals. Millimeter-sized, orange, $MAPbBr_3$ single crystals were grown by heating approximately 1 mL of a 1 M $PbBr_2$/MABr solution in DMF by immersing the vial in silicone oil or directly placing the vial on a hot plate at 80 °C until crystals of the desired size had formed, which typically occurred after 5 to 10 min.[11,13] A new crystal was used as the substrate for every AFM experiment. The 5.0 mm $MAPbBr_3$ single crystal used for Laue back-reflection measurements (Figure S1c) was grown from a seed approximately 1.0 mm in size placed in a 2 mL solution of 1 M $PbBr_2$/MABr in DMF. The vial was immersed in a silicone oil bath and maintained at 70 °C over 4 h.

4.4. In Situ AFM Monitoring. Immediately after removal from the growth solution, each $MAPbBr_3$ crystal was dipped in toluene to minimize surface roughening due to dissolution of the crystals as the solution cools down. Prior to AFM imaging, the newly grown $MAPbBr_3$ crystal was affixed with one drop of polydimethylsiloxane (PDMS; SYLGARD 184 Silicone Elastomer Kit, Dow Corning) to a glass substrate under an optical microscope. The glass coverslip was affixed to a metallic AFM specimen disk (12 mm in diameter, Ted Pella). All in situ crystal growth kinetics were measured by tracking the step movement of $MAPbBr_3$ as a function of time at different constituent and additive concentrations. The images were collected by PeakForce Tapping mode (Bruker, Nanoscope 8, CA) using hybrid probes consisting of silicon tips on silicon nitride cantilevers (AppNano Vscan Air, spring constant k = 0.292 N/m, tip radius <10 nm; http://www.appnano.com/search-products/vscan-air). PeakForce Tapping is a mode where the probe periodically taps the sample, and the interaction force is monitored by the deflection of the cantilever for each pixel. The feedback loop keeps the peak force constant. The images were collected with a scan rate of 2 Hz, a sampling rate of 256 lines/scan, and a scan size of either 40 or 50 μm. The images were collected while supersaturated solutions were injected and kept static in a liquid cell (Bruker). Measurements were made over a range of concentrations of $MAPbBr_3$ (0.94, 1.02, and 1.10 M). During imaging in a supersaturated solution, optical microscopy revealed the appearance of different surface features (i.e., dissolution pits and growth hillocks) at varying temperatures (Figure S2). Well-defined spiral hillocks on the $MAPbBr_3$ {100} facets were first captured by optical microscopy before monitoring step movement by AFM during growth at different temperatures and additive concentrations. Growth rates were determined from data collected shortly after the onset of step movement, where the step movement exhibited a linear dependence on the elapsed time. To study the effect of HCOOH on the step kinetics, growth experiments on $MAPbBr_3$ {100} facets at controlled HCOOH concentrations (4, 5, and 6% by volume ratio to DMF) were performed on the same AFM setup. The temperature was regulated using a temperature-controlled heating stage (Bruker). Data used in our analyses were typically collected within the first 160 s of each experiment.

During the image collection, the scanning angle was carefully changed to make sure the steps were perpendicular to the fast-scanning direction. Under the condition that the steps are perpendicular to the fast-scanning direction, the step velocities can then be determined from these time-resolved images by measuring the angle θ between the hillock's step edges and vertical direction using an established methodology (Figure 1J).[59] Using the measured angle θ, the step velocity (v_s) was calculated for the step trains on both sides of the hillock using the following eq (eq 3):[59]

$$v_s = \frac{S_r \cdot A \cdot \tan\theta}{N} \tag{3}$$

where S_r is the scan rate (in line/second), A is the scan size (in micrometer/frame), and N is the scanning line number per frame (in line/frame).

To ensure that the AFM images were typical representations of the growth kinetics, several protocols need to be followed. First, the imaging force was minimized to the lowest possible force value, which allowed the tip to track the surface to prevent any measurable effect of

https://doi.org/10.1021/acs.cgd.4c00008
Cryst. Growth Des. 2024, 24, 4955−4965

the tip on the growth kinetics. We verified the absence of tip effects by zooming out to a larger scan box and comparing the step rates with those observed for a smaller scan area. Imaging in the same area may result in the transient movement of features with weak binding to the surface. This effect reduces image quality but ensures that the feature size and kinetics are minimally affected. Next, images were also collected at different scan angles, and trace and retrace images were regularly compared, to get rid of the possibility of imaging artifacts induced by tip contamination.

4.5. Solution Preparation for NMR Experiments. Solutions of 1 M $PbBr_2$ and MABr in a 1-to-1 molar ratio were prepared by weighing the salts in air and adding the appropriate volume of solvent (1 mL). The salts were dissolved in 9/1 v/v DMF-d_7 (≥99.5 atom % *D*, Cambridge Isotope Laboratories)/DMF by stirring at room temperature until the solution was completely clear.

4.6. Solution NMR Measurements. Solution NMR measurements were performed on three different Varian DDRS spectrometers (one 17.6 T magnet and two 11.7 T magnets) using broad-band (BBO) probes. The 90° pulse widths were 13 μs for ^{1}H. ^{1}H spectra were collected using 30° pulses with a recycling delay of 20 s for quantitative analysis. ^{1}H diffusion coefficients were measured using a bipolar pulse pair stimulated echo pulse sequence with convection compensation. The typical parameters for ^{1}H DOSY experiments were gradient g = 1.6−34.5 G/cm, number of increments = 16, diffusion gradient duration δ = 2 ms, diffusion delay Δ = 200 ms, gradient stabilization delay = 2 ms, number of scans = 16, and number of scans for steady state = 32. 90 vol %. DMF-d_7 (10 vol % regular DMF) was used for deuterium signal lock, reducing proton radiation damping, and for the quantitative comparison between DMF, MABr, and HCOOH. Typical data analysis of relaxation and diffusion experiments was done directly in VnmrJ software or Mestrenova. For unrestricted and isotropic diffusion, signal attenuation (I vs I_0) is a function of gyromagnetic ratio γ, gradient strength g, gradient duration δ, diffusion time Δ, and diffusion coefficient D according to Stejskal−Tanner equation:[78]

$$I = I_0 \exp(-D\gamma^2 g^2 \delta^2(\Delta - \delta/3)) = I_0 \exp(-Db) \quad (4)$$

$$\ln(I_0/I) = -Db \quad (5)$$

Here, b is the Stejskal−Tanner parameter; $b = \gamma^2 g^2 \delta^2(\Delta - \delta/3)$. The Stejskal−Tanner plot of ln (I_0/I) vs b yields a straight line with a slope of $-D$ for single-component diffusion. 2D NOESY experiments were carried out using the pulse sequence NOESY_zqf1 with ZQ filter = 30 ms, mixing time = 40, 200, and 400 ms, acquisition time = 0.15 s (t_2) and 0.047 s (t_1), number of increments in t_1 = 256, and number of scans = 16. The exchange rate between water and MA^+ can be estimated from the peak volumes from the 2D NOESY spectra.[61,62] 2D peak volume at row i and column j at a mixing time of t_m can be expressed as a function of M_j^0 (the magnetization of the nuclei at site j at equilibrium) and **R** (the rate-constant matrix with the values $R_{ij} = -k_{ji}$, the first-order exchange rate constant from site j to site i: $I_{ij}(t_m) = (e^{-\mathbf{R}t_m})_{ij} M_j^0$. Therefore, the rate-constant matrix can be calculated directly from the peak-volume matrix **A** with $A_{ij} = I_{ij}(t_m)/M_j^0$): $\mathbf{R} = -\ln(\mathbf{A})/t_m$. The rate constant was calculated at each mixing time for three samples with different water contents, and the range of rate constants was reported.

4.7. Laue Back-Reflection X-ray Diffraction to Determine Crystal Orientation. A Multiwire Real-Time Back-Reflection Camera System (MWL120) was used to detect the orientation of a $MAPbBr_3$ single crystal. A tungsten anode was used to generate polychromatic "white" X-rays to simultaneously observe multiple diffraction peaks from the crystal without producing excess characteristic (K or L shell) radiation. The crystal was mounted on a barrel holder orientation base (MWL703) with double-sided tape, and the base of the holder was positioned 146.00 mm from the detector (Figure S1b). A 3.00 mm collimator was placed over the X-ray tube, and the real-time Laue camera was used to orient the crystal growth plane. The diffraction pattern was collected for 20 s and autoindexed by NorthStar 7 software to generate the *hkl* solution.

■ ASSOCIATED CONTENT

Supporting Information

The Supporting Information is available free of charge at https://pubs.acs.org/doi/10.1021/acs.cgd.4c00008.

Laue back-reflection pattern, optical microscopy images of single-crystal surfaces, 2D ^{1}H−^{1}H NOESY spectra, ^{1}H NMR spectrum with more details on the inset of Figure 4B, peak fittings for MA^+ resonances at varying temperatures, kinetic coefficient determination, ^{1}H NMR spectra at varying temperatures, line fit results for the temperature-dependent step velocity data, *A* and *B* parameters from solubility curve fittings, and extrapolated step velocities and solubilities at 45 °C (PDF)

■ AUTHOR INFORMATION

Corresponding Authors

Jinhui Tao − *Physical and Computational Sciences Directorate, Pacific Northwest National Laboratory, Richland, Washington 99354, United States;* orcid.org/0000-0002-1156-9396; Email: Jinhui.Tao@pnnl.gov

Lara A. Estroff − *Department of Materials Science and Engineering and Kavli Institute at Cornell for Nanoscale Science, Cornell University, Ithaca, New York 14853, United States;* orcid.org/0000-0002-7658-1265; Email: lae37@cornell.edu

Authors

Amnon G. Ortoll-Bloch − *Department of Chemistry and Chemical Biology, Cornell University, Ithaca, New York 14853, United States;* Present Address: Department of Chemistry, Bowdoin College, Brunswick, Maine 04011, United States; orcid.org/0000-0001-5789-3274

Ying Chen − *Physical and Computational Sciences Directorate, Pacific Northwest National Laboratory, Richland, Washington 99354, United States;* orcid.org/0000-0001-7417-0991

Emily Hiralal − *Department of Chemistry and Chemical Biology, Cornell University, Ithaca, New York 14853, United States*

Nancy M. Washton − *Physical and Computational Sciences Directorate, Pacific Northwest National Laboratory, Richland, Washington 99354, United States;* orcid.org/0000-0002-9643-6794

Karl T. Mueller − *Physical and Computational Sciences Directorate, Pacific Northwest National Laboratory, Richland, Washington 99354, United States;* orcid.org/0000-0001-9609-9516

James De Yoreo − *Physical and Computational Sciences Directorate, Pacific Northwest National Laboratory, Richland, Washington 99354, United States; Department of Materials Science and Engineering, University of Washington, Seattle, Washington 98195, United States;* orcid.org/0000-0002-9541-733X

Complete contact information is available at: https://pubs.acs.org/10.1021/acs.cgd.4c00008

Notes

The authors declare no competing financial interest.

https://doi.org/10.1021/acs.cgd.4c00008
Cryst. Growth Des. 2024, 24, 4955−4965

■ ACKNOWLEDGMENTS

This work was supported by the U.S. Department of Energy (DOE), Office of Science, Basic Energy Sciences (BES), under Award #DE-SC0022305 (AFM studies; L.A.E and J.T.) and Award KC020105-FWP12152 (NMR studies, Y. C. and J. T.) and a seed research grant from the Cornell Center for Materials Research with funding from the NSF MRSEC program (DMR-1719875) (single-crystal growth, L.A.E). A.G.O−B. gratefully acknowledges the support by the U.S. Department of Energy, Office of Science, Office of Workforce Development for Teachers and Scientists, Office of Science Graduate Student Research (SCGSR) program. The SCGSR program is administered by the Oak Ridge Institute for Science and Education for the DOE under contract number DE-SC0014664. A.G.O−B. also gratefully acknowledges the support received from the Cornell University Graduate School through a Provost Diversity Fellowship. Y.C., N.M.W., and K.T.M. also acknowledge funding supported by the U.S. Department of Energy, Office of Science, Basic Energy Sciences, Division of Materials Sciences and Engineering under Award FWP67554. All NMR experiments were performed using EMSL (grid.436923.9), a DOE Office of Science User Facility sponsored by the Office of Biological and Environmental Research. PNNL is operated by Battelle for the Department of Energy under contract No. DE-AC05-76RLO1830.

■ REFERENCES

(1) NREL best research-cell efficiencies. https://www.nrel.gov/pv/cell-efficiency.html (accessed May 16, 2024).
(2) Shi, D.; Adinolfi, V.; Comin, R.; Yuan, M.; Alarousu, E.; Buin, A.; Chen, Y.; Hoogland, S.; Rothenberger, A.; Katsiev, K.; Losovyj, Y.; Zhang, X.; Dowben, P. A.; Mohammed, O. F.; Sargent, E. H.; Bakr, O. M. Low Trap-State Density and Long Carrier Diffusion in Organolead Trihalide Perovskite Single Crystals. *Science* **2015**, *347* (6221), 519−522.
(3) Dong, Q.; Fang, Y.; Shao, Y.; Mulligan, P.; Qiu, J.; Cao, L.; Huang, J. Electron-Hole Diffusion Lengths > 175 mm in Solution-Grown $CH_3NH_3PbI_3$ Single Crystals. *Science* **2015**, *347* (6225), 967−970.
(4) Capitaine, A.; Sciacca, B. Monocrystalline Methylammonium Lead Halide Perovskite Materials for Photovoltaics. *Adv. Mater.* **2021**, *33* (52), No. 2102588.
(5) Yan, J.; Li, H.; Aldamasy, M. H.; Frasca, C.; Abate, A.; Zhao, K.; Hu, Y. Advances in the Synthesis of Halide Perovskite Single Crystals for Optoelectronic Applications. *Chem. Mater.* **2023**, *35* (7), 2683−2712.
(6) Chen, Z.; Turedi, B.; Alsalloum, A. Y.; Yang, C.; Zheng, X.; Gereige, I.; Alsaggaf, A.; Mohammed, O. F.; Bakr, O. M. Single-Crystal $MAPbI_3$ Perovskite Solar Cells Exceeding 21% Power Conversion Efficiency. *ACS Energy Lett.* **2019**, *4* (6), 1258−1259.
(7) Alsalloum, A. Y.; Turedi, B.; Zheng, X.; Mitra, S.; Zhumekenov, A. A.; Lee, K. J.; Maity, P.; Gereige, I.; AlSaggaf, A.; Roqan, I. S.; Mohammed, O. F.; Bakr, O. M. Low-Temperature Crystallization Enables 21.9% Efficient Single-Crystal $MAPbI_3$ Inverted Perovskite Solar Cells. *ACS Energy Lett.* **2020**, *5* (2), 657−662.
(8) Corzo, D.; Wang, T.; Gedda, M.; Yengel, E.; Khan, J. I.; Li, R.; Niazi, M. R.; Huang, Z.; Kim, T.; Baran, D.; Sun, D.; Laquai, F.; Anthopoulos, T. D.; Amassian, A. A Universal Cosolvent Evaporation Strategy Enables Direct Printing of Perovskite Single Crystals for Optoelectronic Device Applications. *Adv. Mater.* **2022**, *34* (9), No. 2109862.
(9) Wei, W.; Zhang, Y.; Xu, Q.; Wei, H.; Fang, Y.; Wang, Q.; Deng, Y.; Li, T.; Gruverman, A.; Cao, L.; Huang, J. Monolithic Integration of Hybrid Perovskite Single Crystals with Heterogenous Substrate for Highly Sensitive X-Ray Imaging. *Nat. Photonics* **2017**, *11* (5), 315−321.
(10) Wei, H.; Fang, Y.; Mulligan, P.; Chuirazzi, W.; Fang, H. H.; Wang, C.; Ecker, B. R.; Gao, Y.; Loi, M. A.; Cao, L.; Huang, J. Sensitive X-Ray Detectors Made of Methylammonium Lead Tribromide Perovskite Single Crystals. *Nat. Photonics* **2016**, *10* (5), 333−339.
(11) Saidaminov, M. I.; Abdelhady, A. L.; Murali, B.; Alarousu, E.; Burlakov, V. M.; Peng, W.; Dursun, I.; Wang, L.; He, Y.; MacUlan, G.; Goriely, A.; Wu, T.; Mohammed, O. F.; Bakr, O. M. High-Quality Bulk Hybrid Perovskite Single Crystals within Minutes by Inverse Temperature Crystallization. *Nat. Commun.* **2015**, *6*, No. 7586.
(12) Saidaminov, M. I.; Abdelhady, A. L.; Maculan, G.; Bakr, O. M. Retrograde Solubility of Formamidinium and Methylammonium Lead Halide Perovskites Enabling Rapid Single Crystal Growth. *Chem, Commun.* **2015**, *51* (100), 17658−17661.
(13) Nayak, P. K.; Moore, D. T.; Wenger, B.; Nayak, S.; Haghighirad, A. A.; Fineberg, A.; Noel, N. K.; Reid, O. G.; Rumbles, G.; Kukura, P.; Vincent, K. A.; Snaith, H. J. Mechanism for Rapid Growth of Organic-Inorganic Halide Perovskite Crystals. *Nat. Commun.* **2016**, *7*, No. 13303.
(14) Liu, Y.; Yang, Z.; Cui, D.; Ren, X.; Sun, J.; Liu, X.; Zhang, J.; Wei, Q.; Fan, H.; Yu, F.; Zhang, X.; Zhao, C.; Liu, S. F. Two-Inch-Sized Perovskite $CH_3NH_3PbX_3$ (X = Cl, Br, I) Crystals: Growth and Characterization. *Adv. Mater.* **2015**, *27* (35), 5176−5183.
(15) Lian, Z.; Yan, Q.; Gao, T.; Ding, J.; Lv, Q.; Ning, C.; Li, Q.; Sun, J. L. Perovskite $CH_3NH_3PbI_3(Cl)$ Single Crystals: Rapid Solution Growth, Unparalleled Crystalline Quality, and Low Trap Density toward 10^8 cm^{-3}. *J. Am. Chem. Soc.* **2016**, *138* (30), 9409−9412.
(16) Amari, S.; Verilhac, J. M.; Gros D'Aillon, E.; Ibanez, A.; Zaccaro, J. Optimization of the Growth Conditions for High Quality $CH_3NH_3PbBr_3$ Hybrid Perovskite Single Crystals. *Cryst. Growth Des.* **2020**, *20* (3), 1665−1672.
(17) Manser, J. S.; Saidaminov, M. I.; Christians, J. A.; Bakr, O. M.; Kamat, P. V. Making and Breaking of Lead Halide Perovskites. *Acc. Chem. Res.* **2016**, *49* (2), 330−338.
(18) Manser, J. S.; Reid, B.; Kamat, P. V. Evolution of Organic-Inorganic Lead Halide Perovskite from Solid-State Iodoplumbate Complexes. *J. Phys. Chem. C* **2015**, *119* (30), 17065−17073.
(19) Stamplecoskie, K. G.; Manser, J. S.; Kamat, P. V. Dual Nature of the Excited State in Organic-Inorganic Lead Halide Perovskites. *Energy Environ. Sci.* **2015**, *8* (1), 208−215.
(20) Sharenko, A.; Mackeen, C.; Jewell, L.; Bridges, F.; Toney, M. F. Evolution of Iodoplumbate Complexes in Methylammonium Lead Iodide Perovskite Precursor Solutions. *Chem. Mater.* **2017**, *29* (3), 1315−1320.
(21) Hamill, J. C.; Schwartz, J.; Loo, Y. L. Influence of Solvent Coordination on Hybrid Organic-Inorganic Perovskite Formation. *ACS Energy Lett.* **2018**, *3* (1), 92−97.
(22) Radicchi, E.; Mosconi, E.; Elisei, F.; Nunzi, F.; De Angelis, F. Understanding the Solution Chemistry of Lead Halide Perovskites Precursors. *ACS Appl. Energy Mater.* **2019**, *2*, 3400−3409.
(23) Tidhar, Y.; Edri, E.; Weissman, H.; Zohar, D.; Hodes, G.; Cahen, D.; Rybtchinski, B.; Kirmayer, S. Crystallization of Methyl Ammonium Lead Halide Perovskites: Implications for Photovoltaic Applications. *J. Am. Chem. Soc.* **2014**, *136* (38), 13249−13256.
(24) Fateev, S. A.; Petrov, A. A.; Khrustalev, V. N.; Dorovatovskii, P. V.; Zubavichus, Y. V.; Goodilin, E. A.; Tarasov, A. B. Solution Processing of Methylammonium Lead Iodide Perovskite from Gamma-Butyrolactone: Crystallization Mediated by Solvation Equilibrium. *Chem. Mater.* **2018**, *30* (15), 5237−5244.
(25) Moore, D. T.; Sai, H.; Tan, K. W.; Smilgies, D.-M.; Zhang, W.; Snaith, H. J.; Wiesner, U.; Estroff, L. A. Crystallization Kinetics of Organic−Inorganic Trihalide Perovskites and the Role of the Lead Anion in Crystal Growth. *J. Am. Chem. Soc.* **2015**, *137* (6), 2350−2358.
(26) Cao, J.; Jing, X.; Yan, J.; Hu, C.; Chen, R.; Yin, J.; Li, J.; Zheng, N. Identifying the Molecular Structures of Intermediates for

https://doi.org/10.1021/acs.cgd.4c00008
Cryst. Growth Des. 2024, 24, 4955−4965

Optimizing the Fabrication of High-Quality Perovskite Films. *J. Am. Chem. Soc.* **2016**, *138* (31), 9919−9926.
(27) Guo, Y.; Shoyama, K.; Sato, W.; Matsuo, Y.; Inoue, K.; Harano, K.; Liu, C.; Tanaka, H.; Nakamura, E. Chemical Pathways Connecting Lead(II) Iodide and Perovskite via Polymeric Plumbate(II) Fiber. *J. Am. Chem. Soc.* **2015**, *137* (50), 15907−15914.
(28) Heo, J. H.; Song, D. H.; Han, H. J.; Kim, S. Y.; Kim, J. H.; Kim, D.; Shin, H. W.; Ahn, T. K.; Wolf, C.; Lee, T. W.; Im, S. H. Planar $CH_3NH_3PbI_3$ Perovskite Solar Cells with Constant 17.2% Average Power Conversion Efficiency Irrespective of the Scan Rate. *Adv, Mater.* **2015**, *27* (22), 3424−3430.
(29) Eperon, G. E.; Stranks, S. D.; Menelaou, C.; Johnston, M. B.; Herz, L. M.; Snaith, H. J. Formamidinium Lead Trihalide: A Broadly Tunable Perovskite for Efficient Planar Heterojunction Solar Cells. *Energy Environ. Sci.* **2014**, *7* (3), 982−988.
(30) Lang, A.; Polishchuk, I.; Seknazi, E.; Feldmann, J.; Katsman, A.; Pokroy, B. Bioinspired Molecular Bridging in a Hybrid Perovskite Leads to Enhanced Stability and Tunable Properties. *Adv. Funct. Mater.* **2020**, *30* (42), No. 2005136.
(31) Noel, N. K.; Congiu, M.; Ramadan, A. J.; Fearn, S.; McMeekin, D. P.; Patel, J. B.; Johnston, M. B.; Wenger, B.; Snaith, H. J. Unveiling the Influence of pH on the Crystallization of Hybrid Perovskites, Delivering Low Voltage Loss Photovoltaics. *Joule* **2017**, *1* (2), 328−343.
(32) Fan, Z.; Xiao, H.; Wang, Y.; Zhao, Z.; Lin, Z.; Cheng, H. C.; Lee, S. J.; Wang, G.; Feng, Z.; Goddard, W. A.; Huang, Y.; Duan, X. Layer-by-Layer Degradation of Methylammonium Lead Tri-Iodide Perovskite Microplates. *Joule* **2017**, *1* (3), 548−562.
(33) Liu, Y.; Zhang, Y.; Yang, Z.; Feng, J.; Xu, Z.; Li, Q.; Hu, M.; Ye, H.; Zhang, X.; Liu, M.; Zhao, K.; Liu, S. Low-Temperature-Gradient Crystallization for Multi-Inch High-Quality Perovskite Single Crystals for Record Performance Photodetectors. *Mater. Today* **2019**, *22*, 67−75.
(34) Vekilov, P. G. What Determines the Rate of Growth of Crystals from Solution? *Cryst. Growth Des.* **2007**, *7* (12), 2796−2810.
(35) Qiu, S. R.; Orme, C. A. Dynamics of Biomineral Formation at the Near-Molecular Level. *Chem. Rev.* **2008**, *108* (11), 4784−4822.
(36) De Yoreo, J. J.; Vekilov, P. G. Principles of Crystal Nucleation and Growth. *Rev. Mineral Geochem* **2003**, *54* (1), 57−93.
(37) Chernov, A. A. Notes on Interface Growth Kinetics 50 Years after Burton, Cabrera and Frank. *J. Cryst. Growth* **2004**, *264* (4), 499−518.
(38) Chernov, A. A. Growth Mechanisms. In *Modern Crystallography III: Crystal Growth*; Chernov, A. A., Ed.; Springer Berlin Heidelberg: Berlin, Heidelberg, 1984; pp 104−158 .
(39) Woodruff, D. P. How Does Your Crystal Grow? A Commentary on Burton, Cabrera and Frank (1951) "The Growth of Crystals and the Equilibrium Structure of Their Surfaces. *Philos. Trans. R. Soc., A* **2015**, *373* (2039), No. 20140230.
(40) Burton, W. K.; Cabrera, N.; Frank, F. C. The Growth of Crystals and the Equilibrium Structure of Their Surfaces. *Philos. Trans. R. Soc., A* **1951**, *243* (866), 299−358.
(41) Elhadj, S.; De Yoreo, J. J.; Hoyer, J. R.; Dove, P. M. Role of Molecular Charge and Hydrophilicity in Regulating the Kinetics of Crystal Growth. *Proc. Natl. Acad. Sci. USA* **2006**, *103* (51), 19237−19242.
(42) Mijowska, S.; Polishchuk, I.; Lang, A.; Seknazi, E.; Dejoie, C.; Fermani, S.; Falini, G.; Demitri, N.; Polentarutti, M.; Katsman, A.; Pokroy, B. High Amino Acid Lattice Loading at Nonambient Conditions Causes Changes in Structure and Expansion Coefficient of Calcite. *Chem. Mater.* **2020**, *32* (10), 4205−4212.
(43) Lupulescu, A. I.; Rimer, J. D. In Situ Imaging of Silicalite-1 Surface Growth Reveals the Mechanism of Crystallization. *Science* **2014**, *344* (6185), 729−732.
(44) Tao, J.; Lee, M.-S.; Sushko, M. L.; De Yoreo, J. J.; Liu, J.; Zhang, Z.; Banerjee, D.; Akkineni, S.; Bowden, M. E.; Thallapally, P. K.; Shin, Y.; Sinnwell, M. A. Controlling Metal−Organic Framework/ZnO Heterostructure Kinetics through Selective Ligand Binding to ZnO Surface Steps. *Chem. Mater.* **2020**, *32* (15), 6666−6675.
(45) Chen, J.; Zhu, E.; Liu, J.; Zhang, S.; Lin, Z.; Duan, X.; Heinz, H.; Huang, Y.; De Yoreo, J. J. Building Two-Dimensional Materials One Row at a Time: Avoiding the Nucleation Barrier. *Science* **2018**, *362* (6419), 1135−1139.
(46) Shtukenberg, A. G.; Poloni, L. N.; Zhu, Z.; An, Z.; Bhandari, M.; Song, P.; Rohl, A. L.; Kahr, B.; Ward, M. D. Dislocation-Actuated Growth and Inhibition of Hexagonal l-Cystine Crystallization at the Molecular Level. *Cryst. Growth Des.* **2015**, *15* (2), 921−934.
(47) Fukuma, T.; Garcia, R. Atomic- and Molecular-Resolution Mapping of Solid−Liquid Interfaces by 3D Atomic Force Microscopy. *ACS Nano* **2018**, *12* (12), 11785−11797.
(48) Teng, H. H.; Dove, P. M.; Orme, C. A.; De Yoreo, J. J. Thermodynamics of Calcite Growth: Baseline for Understanding Biomineral Formation. *Science* **1998**, *282* (5389), 724−727.
(49) Petsev, D. N.; Chen, K.; Gliko, O.; Vekilov, P. G. Diffusion-Limited Kinetics of the Solution-Solid Phase Transition of Molecular Substances. *Proc. Natl. Acad. Sci. U. S. A.* **2003**, *100* (3), 792−796.
(50) Chakrabarti, R.; Verma, L.; Hadjiev, V. G.; Palmer, J. C.; Vekilov, P. G. The Elementary Reactions for Incorporation into Crystals. *Proc. Natl. Acad. Sci. U.S.A.* **2024**, *121* (7), No. e2320201121.
(51) Thomas, T. N.; Land, T. A.; Martin, T.; Casey, W. H.; De Yoreo, J. J. AFM Investigation of Step Kinetics and Hillock Morphology of the {100} Face of KDP. *J. Cryst. Growth* **2004**, *260* (3−4), 566−579.
(52) Shtukenberg, A. G.; Ward, M. D.; Kahr, B. Crystal Growth with Macromolecular Additives. *Chem. Rev.* **2017**, *117* (24), 14042−14090.
(53) Kadro, J. M.; Nonomura, K.; Gachet, D.; Grätzel, M.; Hagfeldt, A. Facile Route to Freestanding $CH_3NH_3PbI_3$ Crystals Using Inverse Solubility. *Sci. Rep.* **2015**, *5* (1), No. 11654.
(54) Wang, H.; Nan, R.; Jian, Z.; Jin, C.; Wei, Y.; Bai, Y.; Li, H. Step-Controlled Growth of $MAPbBr_3$ Single Crystal and Temperature-Dependent Variations of MA^+ Cations during Nonphase Transition. *Mater. Sci. Semicond. Process.* **2021**, *135*, No. 106107.
(55) Shen, H.; Nan, R.; Jian, Z.; Li, X. Defect Step Controlled Growth of Perovskite $MAPbBr_3$ Single Crystal. *J. Mater. Sci.* **2019**, *54* (17), 11596−11603.
(56) Ghosh, S.; Mishra, S.; Singh, T. Antisolvents in Perovskite Solar Cells: Importance, Issues, and Alternatives. *Adv. Mater. Interfaces* **2020**, *7* (18), No. 2000950.
(57) Poglitsch, A.; Weber, D. Dynamic Disorder in Methylammoniumtrihalogenoplumbates (II) Observed by Millimeter-wave Spectroscopy. *J. Chem. Phys.* **1987**, *87* (11), 6373−6378.
(58) Song, J.; Feng, X.; Li, H.; Li, W.; Lu, T.; Guo, C.; Zhang, H.; Wei, H.; Yang, B. Facile Strategy for Facet Competition Management to Improve the Performance of Perovskite Single-Crystal X-Ray Detectors. *J. Phys. Chem. Lett.* **2020**, *11* (9), 3529−3535.
(59) Teng, H. H.; Dove, P. M.; De Yoreo, J. J. Kinetics of Calcite Growth: Surface Processes and Relationships to Macroscopic Rate Laws. *Geochim. Cosmochim. Acta* **2000**, *64* (13), 2255−2266.
(60) Vekilov, P. G.; Ataka, M.; Katsura, T. Laser Michelson Interferometry Investigation of Protein Crystal Growth. *J. Cryst. Growth* **1993**, *130* (1−2), 317−320.
(61) Macura, S.; Ernst, R. R. Elucidation of Cross Relaxation in Liquids by Two-Dimensional N.M.R. Spectroscopy. *Mol. Phys.* **1980**, *41* (1), 95−117.
(62) Perrin, C. L.; Gipe, R. K. Multisite Kinetics by Quantitative Two-Dimensional NMR. *J. Am. Chem. Soc.* **1984**, *106* (14), 4036−4038.
(63) Nicholson, S. T.; Roberts, K. J.; Izumi, T.; Lai, X. Characterization of Mass Transfer within the Crystal-Solution Boundary Layer of L-Alanine {120} Faces Using Laser Interferometry during Growth and Dissolution. *Cryst. Growth Des.* **2023**, *23* (4), 2755−2769.
(64) Darkins, R.; McPherson, I. J.; Ford, I. J.; Duffy, D. M.; Unwin, P. R. Critical Step Length as an Indicator of Surface Supersaturation during Crystal Growth from Solution. *Cryst. Growth Des.* **2022**, *22* (2), 982−986.

https://doi.org/10.1021/acs.cgd.4c00008
Cryst. Growth Des. 2024, 24, 4955−4965

(65) Chen, G.; Liu, X.; An, J.; Wang, S.; Zhao, X.; Gu, Z.; Yuan, C.; Xu, X.; Bao, J.; Hu, H.-S.; Li, J.; Wang, X. Nucleation-Mediated Growth of Chiral 3D Organic−Inorganic Perovskite Single Crystals. *Nat. Chem.* **2023**, *15* (11), 1581−1590.
(66) Shtukenberg, A. G.; Ward, M. D.; Kahr, B. Crystal Growth Inhibition by Impurity Stoppers, Now. *J. Cryst. Growth* **2022**, *597*, No. 126839.
(67) Qiu, S. R.; Wierzbicki, A.; Salter, E. A.; Zepeda, S.; Orme, C. A.; Hoyer, J. R.; Nancollas, G. H.; Cody, A. M.; De Yoreo, J. J. Modulation of Calcium Oxalate Monohydrate Crystallization by Citrate through Selective Binding to Atomic Steps. *J. Am. Chem. Soc.* **2005**, *127* (8), 9036−9044.
(68) Ma, W.; Lutsko, J. F.; Rimer, J. D.; Vekilov, P. G. Antagonistic Cooperativity between Crystal Growth Modifiers. *Nature* **2020**, *577* (7791), 497−501.
(69) Orme, C. A.; Noy, A.; Wierzbicki, A.; Mcbride, M. T.; Grantham, M.; Teng, H. H.; Dove, P. M.; Deyoreo, J. J. Formation of Chiral Morphologies through Selective Binding of Amino Acids to Calcite Surface Steps. *Nature* **2001**, *411* (6839), 775−779.
(70) Davis, K. J.; Dove, P. M.; De Yoreo, J. J. The Role of Mg^{2+} as an Impurity in Calcite Growth. *Science* **2000**, *290* (5494), 1134−1137.
(71) Chung, J.; Granja, I.; Taylor, M. G.; Mpourmpakis, G.; Asplin, J. R.; Rimer, J. D. Molecular Modifiers Reveal a Mechanism of Pathological Crystal Growth Inhibition. *Nature* **2016**, *536* (7617), 446−450.
(72) Chen, C. L.; Qi, J.; Zuckermann, R. N.; De Yoreo, J. J. Engineered Biomimetic Polymers as Tunable Agents for Controlling $CaCO_3$ mineralization. *J. Am. Chem. Soc.* **2011**, *133* (14), 5214−5217.
(73) Feng, G.; Huang, J.; Sumpter, B. G.; Meunier, V.; Qiao, R. Structure and Dynamics of Electrical Double Layers in Organic Electrolytes. *Phys. Chem. Chem. Phys.* **2010**, *12* (20), 5468−5479.
(74) Marenich, A. V.; Kelly, C. P.; Thompson, J. D.; Hawkins, G. D.; Chambers, C. C.; Giesen, D. J.; Winget, P.; Cramer, C. J.; Truhlar, D. G. *Minnesota Solvation Database − Version 2012*: Minneapolis, 2012
(75) Thompson, J. D.; Cramer, C. J.; Truhlar, D. G. New Universal Solvation Model and Comparison of the Accuracy of the SM5.42R, SM5.43R, C-PCM, D-PCM, and IEF-PCM Continuum Solvation Models for Aqueous and Organic Solvation Free Energies and for Vapor Pressures. *J. Phys. Chem. A* **2004**, *108* (31), 6532−6542.
(76) Zambelli, S. Chemical Kinetics, an Historical Introduction: Croatia, 2012 www.intechopen.com.
(77) Levitt, M. H. *Spin Dynamics: Basics of Nuclear Magnetic Resonance*, 2nd ed.; John Wiley & Sons Ltd: Chichester, West Sussex, England, 2008.
(78) Stejskal, E. O.; Tanner, J. E. Spin Diffusion Measurements: Spin Echoes in the Presence of a Time-Dependent Field Gradient. *J. Chem. Phys.* **1965**, *42* (1), 288−292.

https://doi.org/10.1021/acs.cgd.4c00008
Cryst. Growth Des. 2024, 24, 4955−4965